

See discussions, stats, and author profiles for this publication at: <https://www.researchgate.net/publication/257299828>

Hydrolytically degradable polymer micelles for drug delivery: A SAXS/SANS kinetic study

ARTICLE *in* BIOMACROMOLECULES · OCTOBER 2013

Impact Factor: 5.75 · DOI: 10.1021/bm401186z · Source: PubMed

CITATIONS

10

READS

181

12 AUTHORS, INCLUDING:



[Tomas Etrych](#)

Academy of Sciences of the Czech Republic

64 PUBLICATIONS 2,175 CITATIONS

[SEE PROFILE](#)



[Aurel Radulescu](#)

Forschungszentrum Jülich

128 PUBLICATIONS 979 CITATIONS

[SEE PROFILE](#)



[Karel Ulbrich](#)

Academy of Sciences of the Czech Republic

319 PUBLICATIONS 11,301 CITATIONS

[SEE PROFILE](#)

[Petr Stepanek](#)

Academy of Sciences of the Czech Republic

170 PUBLICATIONS 2,307 CITATIONS

[SEE PROFILE](#)

Hydrolytically Degradable Polymer Micelles for Drug Delivery: A SAXS/SANS Kinetic Study

Sergey K. Filippov,^{*,†} John M. Franklin,[‡] Petr V. Konarev,^{*,‡} Petr Chytil,[†] Tomas Etrych,[†] Anna Bogomolova,[†] Margarita Dyakonova,[§] Christine M. Papadakis,[§] Aurel Radulescu,^{||} Karel Ulbrich,[†] Petr Stepanek,[†] and Dmitri I. Svergun[‡]

[†]Institute of Macromolecular Chemistry, AS CR, Heyrovsky Sq. 2, Prague, Prague 6, 162 06, Czech Republic

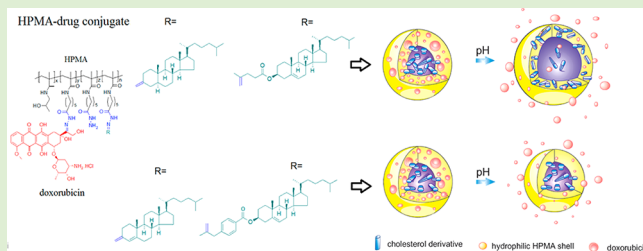
[‡]European Molecular Biology Laboratory, EMBL c/o DESY, Notkestrasse 85, Hamburg, D-22603, Germany

[§]Technische Universität München, Physik-Department, Fachgebiet Physik weicher Materie, James-Franck-Str. 1, 85748 Garching, Germany

^{||}Forschungszentrum Jülich GmbH, Jülich Centre for Neutron Science JCNS, Lichtenbergstraße 1, 85748 Garching, Germany

Supporting Information

ABSTRACT: We report kinetic studies of therapeutically highly potent polymer–drug conjugates consisting of amphiphilic *N*-(2-hydroxypropyl) methacrylamide (HPMA)-based copolymers bearing the anticancer drug doxorubicin (Dox). Highly hydrophobic cholesterol moieties as well as the drug were attached to the polymer backbone by a pH-sensitive hydrazone bond. Moreover, the structure of the spacer between the polymer carrier and the cholesterol moiety differed in order to influence the release rate of the hydrophobic moiety, and thus the disintegration of the high-molecular-weight micellar nanoparticle structure. We performed time-dependent SAXS/SANS measurements after changing pH from a typical blood value (pH 7.2) to that of tumor cells (pH 5.0) to characterize the drug release and changes in particle size and shape. Nanoparticles composed of the conjugates containing Dox were generally larger than the drug-free ones. For most conjugates, nanoparticle growth or decay was observed in the time range of several hours. It was established that the growth/decay rate and the steady-state size of nanoparticles depend on the spacer structure. From analytical fitting, we conclude that the most probable structure of the nanoparticles was a core–shell or a core with attached Gaussian chains. We concluded that the spacer structure determined the fate of a cholesterol derivative after the pH jump. Fitting results for 5α -cholestane-3-onecholestane-3-one and cholestry-4-oxopentanoate (Lev-chol) implied that cholesterol moieties continuously escape from the core of the nanoparticle core and concentrate in the hydrophilic shell. In contrast, cholest-4-en-3-one spacer prevent cholesterol escaping. Dox moiety release was only observed after a change in pH. Such findings justify the model proposed in our previous paper. Lastly, the cholestryl 4-(2-oxopropyl)benzoate (Opb-Chol) was a different case where after the release of hydrophobic Opb-Chol moieties, the core becomes more compact. The physicochemical mechanisms responsible for the scenarios of the different spacers are discussed.



INTRODUCTION

Polymer therapeutics is one of the most challenging and promising trends in biomedical technology.^{1–3} Polymer drug carriers based on *N*-(2-hydroxypropyl)methacrylamide (HPMA) copolymers have been developed for the treatment of tumors, with a special focus on site-specific delivery and controlled release of anticancer agents into tumor tissues or cells.^{4–7} Such interest demands the knowledge of the detailed interior structure of the polymeric nanoparticles and structure evolution during drug delivery. Amphiphilic HPMA-based polymer drug carriers with anticancer drug doxorubicin (Dox) demonstrate promising results, exhibiting enhanced tumor accumulation and excellent antitumor activity in the treatment of solid tumors.⁸ Here, a copolymer containing Dox is bound via a pH-sensitive hydrazone bond and a defined

amount of hydrophobic moieties, among other cholesterol. Recently, we have reported a rigorous, detailed structural investigation of nanoparticles that were composed of the cholesterol bearing polymer carriers and their conjugates with Dox.⁹

Our study of dilute aqueous solutions of conjugates in phosphate buffer at pH 5.0 and 7.2 proves that the content of cholesterol has a strong influence on the size and structure of the system. We established that the presence of even a small amount of cholesterol results in the formation of anisotropic nanoparticles. The results show that the size, anisotropy, and

Received: August 7, 2013

Revised: September 25, 2013

Published: October 1, 2013

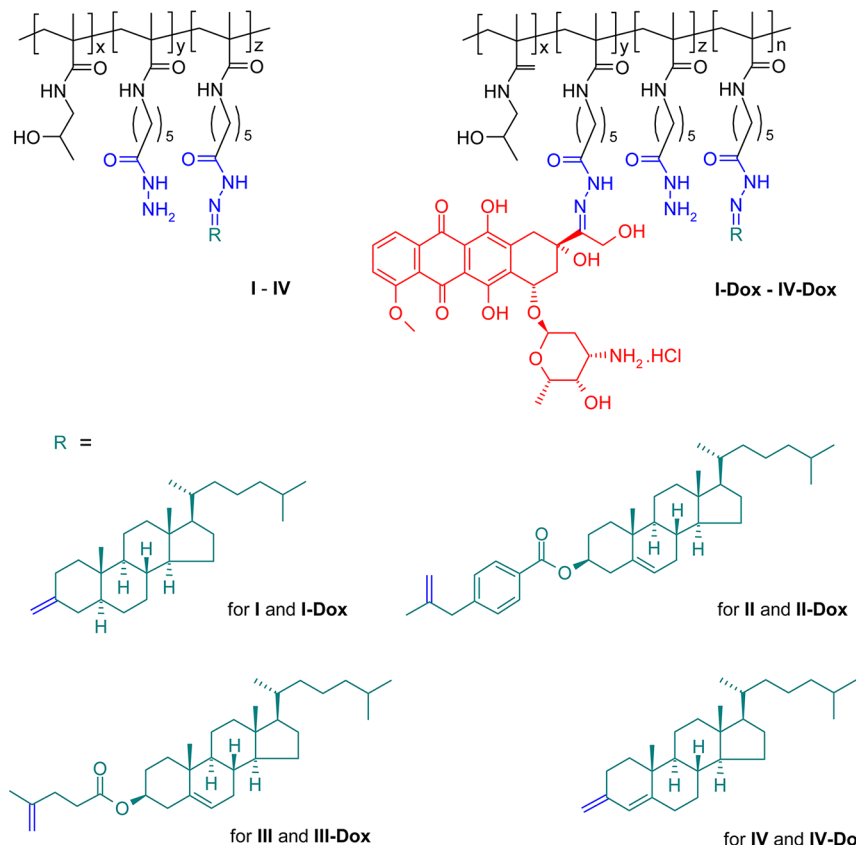


Figure 1. Schematic structures of the hydrophobic moieties. Left part: polymers without Dox; right part: polymers with Dox. The HPMA backbone is in black, the hydrazone bond is in blue, the conjugate moieties are in green, and Dox is in red.

aggregation number, N_{agg} , of the nanoparticles increase with the number of cholesterol moieties. From small-angle X-ray and neutron scattering (SAXS, SANS) experiments, followed by ab initio calculations, we conclude that the most probable structure of HPMA copolymer-cholesterol nanoparticles is a pearl necklace with ellipsoidal pearls mainly composed of cholesterol covered by an HPMA copolymer shell; the pearls are connected by bridges composed of hydrophilic HPMA copolymer chains. Variation in pH perturbs the structure of the nanoparticle only slightly. Using a combination of various techniques, we have demonstrated that Dox moieties are not only embedded inside the cholesterol domain but are also uniformly distributed around the entire nanoparticle, including the hydrophilic HPMA copolymer shell surface.⁹ There are few similar studies for clinically relevant systems, except for recent works by Paul et al.^{7,10,11}

The strong dependence of the size, anisotropy, and aggregation number, N_{agg} , of the nanoparticles on the number of cholesterol moieties show that cholesterol tightly bound to the polymer backbone is crucial for the existence and steady-state properties of the HPMA copolymer-cholesterol nanoparticles. Thus, the following question arise: Are the structures of the cholesterol-HPMA linkage and cholesterol itself important for the nanoparticle formation and behavior in solution? The variation of the cholesterol chemical structure and nature of the linkage could elucidate the answers.

Here, we present the kinetic and steady-state physicochemical properties of supramolecular polymer drug carriers and their conjugates with Dox containing hydrophobic moieties – derivatives of cholesterol: steroid ketones cholest-4-en-3-one and 5 α -cholestane-3-one and esters of oxoacids with cholesterol

cholest-5-en-3 β -yl 4-(2-oxopropyl)benzoate (Opb-Chol) and cholest-5-en-3 β -yl 4-oxopentanoate (Lev-Chol). All cholesterol-derivatives were bound by pH-sensitive hydrolyzable hydrazone bonds and differed in the chemical structure in the vicinity of the bond. The presence of biodegradable linkages between hydrophilic and hydrophobic components of the polymer carriers is advantageous. Degradation of the linkage in the mildly acidic environment of tumor cells results in disintegration and dissolution of the supramolecular structure, thus, facilitating renal removal of the polymer carrier system from the body after successful delivery of its cargo. Recently, we described synthesis and preliminary physicochemical characterization of these conjugates.¹² In the present work, the overall properties and the internal structure of the new copolymers was investigated as a function of time by SAXS/SANS after a sudden change in pH from 7.2 to 5. Subsequently, the mechanisms of the nanoparticle transformations were analyzed. In contrast to our previous studies, less hydrophobic pH-responsive HPMA copolymers (see Figure 1 for monomer structures) were synthesized and used for the experiments. All copolymers had nearly the same content of cholesterol derivatives.

SAMPLES AND METHODS

Synthesis of Polymer–Dox Conjugates and Their Polymer Precursors. Polymer–Dox conjugates and their polymer precursors were prepared according to ref 12. Four different hydrophobic cholesterol-derived moieties varying in the structure close to their keto group, which is used for formation of the hydrolyzable hydrazone bond, were employed.

Table 1. Physico-Chemical Characteristics of the Polymers

sample	structure of hydrophobic substituent	<i>z</i> (content of hydrophobic moieties), mol %	content of Dox, wt %	<i>M</i> _w , g/mol	<i>M</i> _w / <i>M</i> _n	log <i>P</i> value of the spacer
I	5α-cholestan-3-one	1.45	0	23600	1.85	9.0
I-Dox	5α-cholestan-3-one	1.45	10.0	26600	1.88	9.0
II	Opb-Chol	1.25	0	24300	1.96	10.7
II-Dox	Opb-Chol	1.25	10.0	30700	1.65	10.7
III	Lev-Chol	1.25	0	22100	1.88	9.0
III-Dox	Lev-Chol	1.25	9.8	28500	1.89	9.0
IV	cholest-4-en-3-one	1.23	0	24300	1.70	8.5
IV-Dox	cholest-4-en-3-one	1.23	9.8	26800	1.72	8.5

¹ *z* mol % means that *z* monomers from 100 of backbone monomers have a hydrophobe. Molar concentration of Dox is 4.9–5 mol %.

The keto-derivatives used were the following: (I) 5α-cholestan-3-one, (II) cholest-5-en-3β-yl 4-(2-oxopropyl)benzoate (Opb-Chol), (III) cholest-5-en-3β-yl 4-oxopentanoate (Lev-Chol), and (IV) cholest-4-en-3-one. The structure and physicochemical characteristics of all copolymers are shown in Figure 1 and Table 1.

SAXS. SAXS experiments have been previously successfully used for characterization of nanoparticles.^{13–15}

Synchrotron SAXS experiments were performed at the EMBL beamline X33 (DESY, Hamburg, Germany)¹⁶ using a pixel detector (1M PILATUS). The X-ray scattering images were recorded for a sample-detector distance 2.7 m, using a monochromatic incident X-ray beam ($\lambda = 0.15$ nm) covering the range of momentum transfer $0.09 \text{ nm}^{-1} < q < 6.0 \text{ nm}^{-1}$ ($q = 4\pi \sin \theta/\lambda$, where 2θ is the scattering angle). Most of the samples had no measurable radiation damage detected by comparison of eight successive time frames with 15 s exposures. In all the cases reported in this paper, the two-dimensional scattering patterns were isotropic. They were azimuthally averaged to yield the dependence of the scattered intensity $I_s(q)$ on the momentum transfer q . Prior to fitting analysis, the solvent scattering had been subtracted.

All data manipulations were performed using the PRIMUS software.¹⁷ The forward scattering $I_s(q = 0)$, and the radius of gyration R_g were evaluated using the Guinier approximation.¹⁸ These parameters were also computed from the entire scattering patterns using GNOM,¹⁹ which provides the pair-distance distribution functions [PDDF(r)] from which the shape of the nanoparticles, the Porod volume, and the maximum particle dimension (D_{\max}) were determined. DAMMIF,²⁰ a fast version of DAMMIN,²¹ was used to make low-resolution ab initio shape reconstructions of the nanoparticles. The results of 10 DAMMIF runs were averaged to determine common structural features using DAMAVER²² and SUPCOMB.²³ Prior to the DAMMIN/DAMMIF calculation, an appropriate constant was subtracted from each data point to force the q^{-4} decay of the intensity at higher angles following Porod's law²⁴ for homogeneous particles with a smooth surface. This procedure yields a "shape scattering" curve corrected for the unwanted scattering contribution from the internal structure. For further modeling, the data was brought to absolute scale by subtracting an empty cell measurement from a pure water measurement, and scaling by the ratio of the theoretical forward scattering of water²⁵ and the experimental forward scattering intensity of water.

To fit the experimental data we applied a model of a homogeneous spherical core with attached Gaussian coils^{26,27} which is implemented in the SASFit software.²⁸ The most important fitting parameters in this model are R_{core} , the radius

of the spherical core, R_{chain} , the radius of gyration of the chains, r_c , the excess scattering length of a block in the core, r_s : excess scattering length of a block in the chain (for visual explanation, see the inset to Figure 7). In this model, $r_s = V_{\text{pol}} \cdot (\text{SLD}_{\text{shell}} - \text{SLD}_{\text{buffer}})$; $r_c = V_{\text{core}} \cdot (\text{SLD}_{\text{core}} - \text{SLD}_{\text{buffer}})$, where $\text{SLD}_{\text{shell}}$, SLD_{core} , and $\text{SLD}_{\text{buffer}}$ are scattering length densities of shell, core, and buffer, respectively. V_{pol} and V_{core} are the volumes of a polymer chain and a core. As an initial guess for the fitting parameters R_{core} and R_{chain} the results from the above-described model-independent calculations were used. The excess scattering lengths were fitted without a priori information.

SANS. SANS experiments were performed at FRM II on the KWS-2 beamline. Measurements were made on a 128×128 multidetector (pixel size $0.5 \times 0.5 \text{ cm}^2$) using a nonpolarized, monochromatic (wavelength λ set by a velocity selector) incident neutron beam collimated with rectangular apertures for two sample-to-detector distances, namely, 2 and 8 m (with $\lambda = 0.6$ nm). With this setup, the investigated q -range was 0.06 to 3 nm^{-1} . In all cases, the two-dimensional scattering patterns were isotropic and were azimuthally averaged resulting in the dependence of the scattered intensity $I_s(q)$ on q . The curves were corrected for background scattering and detector efficiency. The intensities of neutron scattering are given in arbitrary units. All polymers were used as is without deuteration and dissolved in D₂O. The stopped-flow rapid-mixing technique (BioLogic SFM-400) permitted precise control over the mixing conditions, variable flow rate, and small mixing volumes of polymer solutions and HCl.

Dynamic Light Scattering (DLS). Measurements were carried out on an ALV instrument equipped with a 22 mW He–Ne laser at the angle 90° . The obtained correlation functions were analyzed by REPES,²⁹ an analytical software providing the distribution function of hydrodynamic radii, $G(R_h)$. To account for the logarithmic scale on the R_h axis, all DLS distribution diagrams are shown in the equal area representation, $R_h G(R_h)$.³⁰ In all experiments, about 2 mL of the sample solution was filtered by 0.22 μm PVDF filter and transferred to a sealed dust-free light-scattering cell. The temperature was controlled within 0.05 °C. The apparent hydrodynamic radius of the nanoparticles, R_h , was calculated using the Stokes–Einstein equation.

pH Jump Experiment. All polymers were dissolved in PBS buffer with pH 7.4. pH jump experiments were conducted in two different scenarios. For SANS measurements, a stopped flow device was used. To induce a sharp change in pH from 7.4 to 5.0 for SAXS experiments, a defined amount of 0.1 M HCl was pipetted into a vial with polymer PBS solution. The required amount of 0.1 M HCl was calculated from a calibration curve that was measured for all polymers. Both

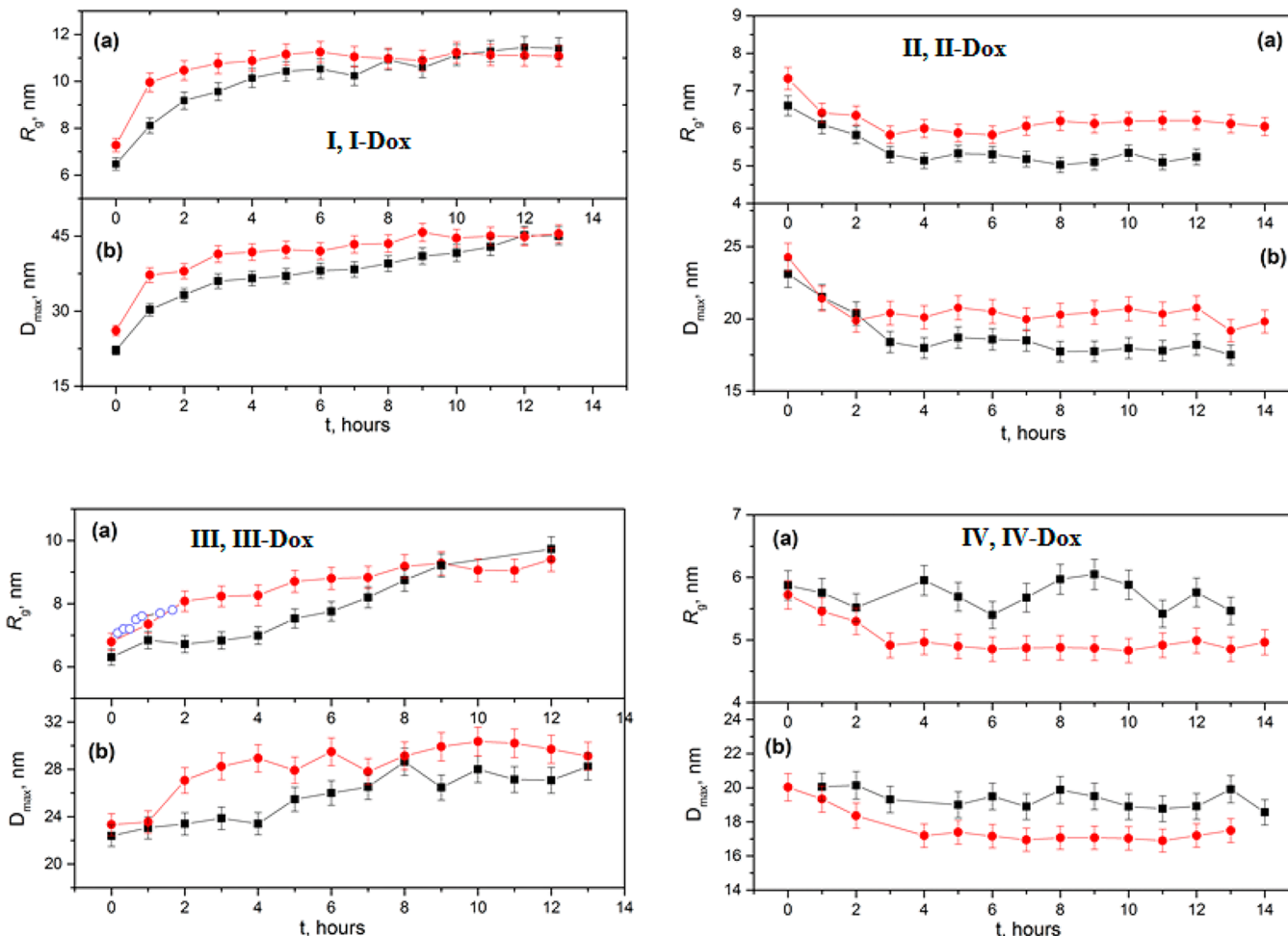


Figure 2. From SAXS. Top left: time dependence of R_g (a), and D_{max} (b) for the conjugates I (●) and I-Dox (red circle). Top right: the conjugates II (●) and II-Dox (red circle). Bottom left: the conjugates III (●, SAXS; ○, SANS) and III-Dox (red circle). Bottom right: the conjugates IV (●) and IV-Dox (red circle). Time was counted from the moment of adding 0.1 M HCl, which changed the pH of the solution from 7.2 to 5.

the SAXS and SANS kinetic experiments were carried out at room temperature, 25 °C.

RESULTS

Synthesis of Polymer–Drug Conjugates and Their Polymer Precursors. The synthesis of amphiphilic HPMA-based polymer carriers and polymer-Dox conjugates was described in detail recently.¹² Keto-derivatives cholest-4-en-3-one, Δ^5 -cholest-3-one, Opb-Chol, and Lev-Chol were selected regarding their influence on the release rate of the hydrazone bond linking them to polymer backbone. Results of the derivative release rates were discussed previously.¹² For further studies, only polymers containing about 1.3 mol % of hydrophobic moiety were used because of their suitable physicochemical properties for subsequent in vivo experiments of therapeutic efficacy.

Shape and Solution Properties (SAXS). To investigate the spatial structure of nanoparticles in solution, we performed SAXS experiments at concentrations of 1×10^{-2} g·mL⁻¹ for all polymers (representative SAXS curves see Figure 1S in the Supporting Information). The pH was changed from 7.2 to 5 by adding a drop of 0.1 M HCl; this defined the time zero, and SAXS measurements were started.

Kinetic Changes of the Overall Size of the Nanoparticles upon Change of pH. To gain overall information

about the size of the nanoparticles, a Guinier analysis of the low- q range was carried out. The extracted R_g and D_{max} values are presented in Figure 2 for all samples (Porod volume values are shown in Figure 2S). Several features should be noted. First, for all copolymers, disregarding the presence of Dox, nanoparticle transformation (growth or disintegration) takes place in the time range of several hours. Second, the growth/decay rate and steady-state size of nanoparticles depend on the spacer structure of the cholesterol derivative (Figure 2). Finally, the R_g values of the nanoparticles composed of the conjugates with doxorubicin particles are generally higher than the ones of the Dox-free ones, with the exception of the conjugates with cholest-4-en-3-one derivative (IV), where the reverse situation was observed.

Shape of the Nanoparticles (Pair Distribution Function Analysis). Time evolution of PDDFs calculated by the GNOM software of the nanoparticle structures is shown in Figure 3. The PDDF is given by the inverse Fourier transformation of the form factor $P(q)$ of a nanoparticle. The PDDF curve obtained from such analysis is structure-sensitive, with theoretically known curve shapes for different model structures.²⁴

From Figure 3, we conclude that the structure of the nanoparticles depends significantly on the nature of the spacer between the polymer carrier and the cholesterol moiety. The

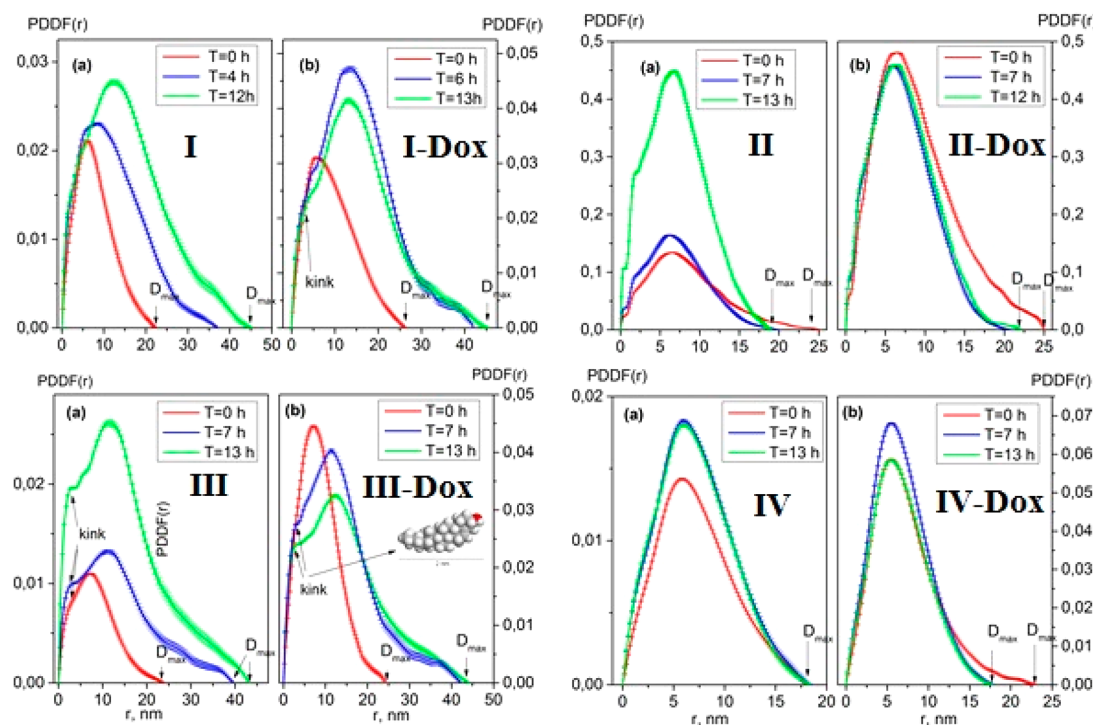


Figure 3. PDDF curves for the polymers and their conjugates for selected times after the pH change from 7.2 to 5.0. The times are indicated in the figure. Top left: polymers I (a) and I-Dox (b). Top right: polymers II (a) and II-Dox (b). Bottom left: polymers III (a) and III-Dox (b). Inset: 3D geometrical configuration of cholesterol. Bottom right: polymers IV (a) and IV-Dox(b). From SAXS.

curves for I, I-Dox, III, and III-Dox conjugates show a pronounced peak at low r values that is followed by asymmetric tails for higher r values. Such a profile may indicate an elongated nanoparticle shape. The PDDF curves clearly show that the maximum dimension of nanoparticles, D_{\max} , which is given by the r value where the PDDF becomes zero, increased with time (Figure 3, top left and bottom left), which is in agreement with the R_g data reported above (Figure 2, top left and bottom left). In contrast, a symmetric bell shape is observed for conjugates IV and IV-Dox that is characteristic of globular conformations (Figure 3, bottom right). D_{\max} decreases or remains nearly constant with time, in agreement with the behavior of R_g (Figure 2, bottom right). The same holds for II and II-Dox.

It is worth mentioning that the shape of the PDDF function for conjugates II, II-Dox, IV, and IV-Dox stays roughly constant over time. From Figure 3 (top right and bottom right) we concluded that the spacer structure of the nanoparticles composed from such conjugates was only slightly evolving.

More interesting time evolution was witnessed for conjugates I, I-Dox, III, and III-Dox. The PDDF maximum shifts to higher values, which was in agreement with the R_g increase reported earlier; moreover, a new shoulder starts to grow at $r = 2.5–3$ nm (Figure 3, top left and bottom left). For conjugate III the shoulder is well resolved and seen as an individual peak (Figure 3, bottom left (a)). By comparison of PDDF functions with and without Dox, it was clear that the evolution of the structure proceeded in the same way. The presence of Dox had only a minor influence on the shape of nanoparticles.

Ab Initio Shape Reconstructions. Despite the fact that we obtained the overall information about the size of the nanoparticles, detailed knowledge of the nanoparticle structure is still missing. We utilized the ab initio program DAMMIN^{21,31} for the reconstruction of the particle shape and the internal

structure from small-angle scattering curve. This model begins with a sphere of densely packed dummy scattering centers. By means of subsequent annealing³² of those scattering centers, a configuration is found that fits the scattering curve. An advantage of this approach is that such calculations require no a priori knowledge of the particle architecture. The only parameter required for the simulation is the maximum particle size, D_{\max} . The ab initio calculations are based on several assumptions. The most important one is the lack of polydispersity. Because we cannot completely discard possible polydispersity of such objects, the results presented below will be regarded as approximations.

Results from the ab initio calculations (DAMMIN/DAMMIF) of our nanoparticles are shown in Figures 3S–5S. Obtained results implied that the hypothetical structure of the nanoparticles composed of conjugate I was a core with attached bulk entities (Figure 3S). The structures of conjugate I and I-Dox converged to a similar shape over time (Figure 5S). Substitution of the 5 α -cholestane-3-one (I) derivative with cholestan-4-en-3-one (IV) changed the 3D structure of nanoparticles dramatically to a compact shape without any bulk subunits (Figure 4S).

Having obtained this model-independent information, we attempted to fit the scattered curves using an approximate model. We neglected interparticle interactions due to rather low concentration of solutions, so $I(q) = P(q)$, where $P(q)$, is a nanoparticle form-factor. The best fit was obtained with a model of a homogeneous spherical core with attached Gaussian coils.^{26,27}

Figures 4–6 show the scattering curves and the fits for different conjugates. For all conjugates, we were able to successfully fit scattering curves by the model. The r_s and r_c fitting parameters are presented in Table 2 and Figure 7 for the two extreme times of 0 and 12/13 h. The excess scattering

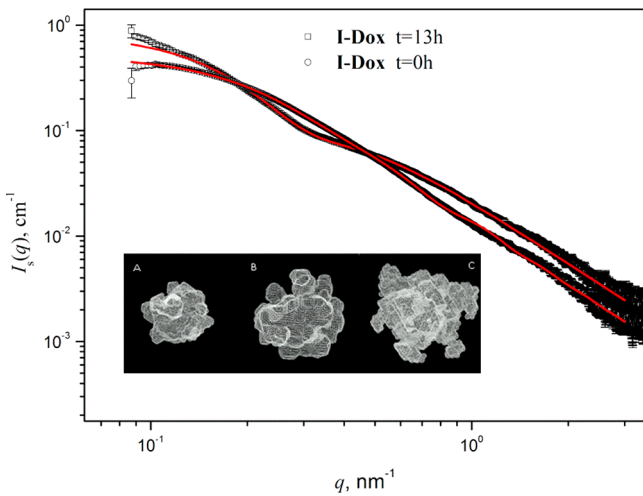


Figure 4. SAXS curves for the conjugate I-Dox as a function of time after the pH jump. Solid lines are fits by a model for a homogeneous sphere with attached Gaussian chains.^{26,27} Inset: Ab initio calculations for the conjugate I-Dox: (A) 0, (B) 7, and (C) 13 h.

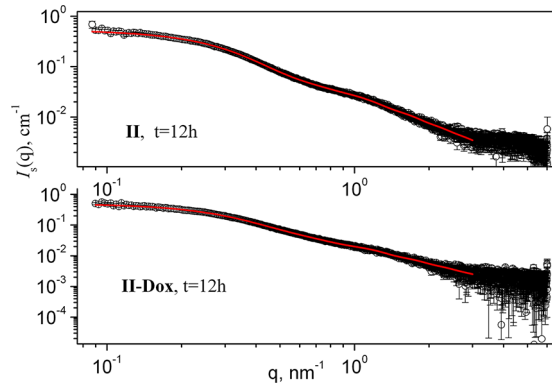


Figure 5. SAXS curves for conjugates II and II-Dox taken 12 h after the change of pH. Solid lines are fits by a model for a homogeneous sphere with attached Gaussian chains.^{26,27}

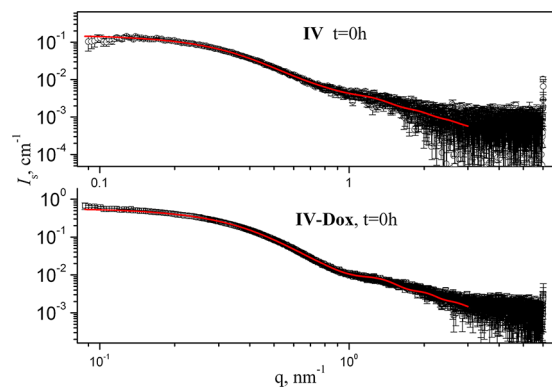


Figure 6. SAXS curves for the conjugates IV and IV-Dox, $t = 0$ h. Solid lines are fits by a model for a homogeneous sphere with attached Gaussian chains.^{26,27}

lengths for core and shell are truly time-dependent and undoubtedly sensitive to the presence of Dox (Figure 7). A polydispersity factor was not implemented into the fitting procedure since the fitting quality was sufficient to describe the entire data range. Attempts to fit the data to a micelle, core–shell, or core–shell with exponential decay density model

Table 2. Fitting Parameters of SAXS Curves for Different Conjugates^a

Sample	T, hours	R_{core} nm	R_{chain} nm	r_c , core excess scat. length, nm	r_s , chain excess scat. length, nm
I	0	5.14	2.63	1.92	1.64
I	7	6.77	3.42	0.94	2.04
I	12	6.76	3.29	0.64	1.83
I-Dox	0	5.46	4.08	2.18	2.84
I-Dox	7	8.48	3.42	1.03	2.06
I-Dox	12	7.81	3.28	0.67	1.79
II	0	5.46	2.69	1.64	1.29
II	7	5.65	2.42	2.85	1.78
II	12	5.50	2.32	3.69	2.75
II-Dox	0	5.20	3.12	2.31	1.96
II-Dox	7	5.07	2.59	2.84	2.41
II-Dox	13	5.20	2.67	2.96	2.50
III	0	5.84	2.62	1.59	1.51
III	7	6.05	2.90	0.40	1.36
III	12	6.43	2.92	0.56	1.95
III-Dox	0	4.43	2.80	0.79	1.37
III-Dox	7	6.18	3.33	0.62	2.19
III-Dox	13	6.58	3.22	0.50	2.12
IV	0	4.79	2.28	0.97	0.78
IV	7	4.74	2.12	0.89	0.89
IV	13	4.92	2.24	1.18	1.06
IV-Dox	0	4.50	2.18	1.48	1.02
IV-Dox	7	4.27	1.96	1.20	1.08
IV-Dox	12	4.28	1.94	1.17	1.13

^aThe numbers marked in grey highlight the drastic time changes of r_s and r_c .

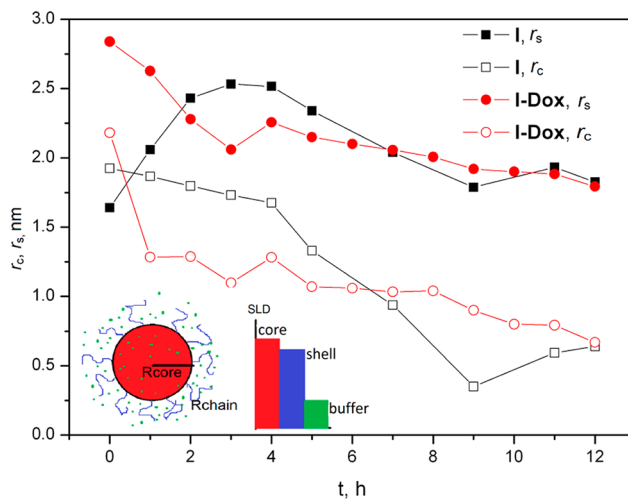


Figure 7. Excess scattering lengths r_c and r_s of the core and the shell from model fitting as a function of time for conjugates I and I-Dox. Inset: cartoon of the applied model.

without polydispersity failed. Nevertheless, we admit that other models that topologically resemble our model could also be used if polydispersity would be involved into the fitting (e.g., a core with attached Gaussian coils model may not be distinguishable from a core–shell model with exponential decay density in a polydisperse shell). One can see that time behavior of fitting parameters was in qualitative agreement with

the behavior of model independent parameters, for example, R_g reported above (Table 2, Figure 2). Assuming that $R_g = R_{\text{core}} + R_{\text{shell}}$, which is not perfectly true, one can see that there is semiquantitative agreement between data from model fitting and model-independent data. Again, the spacer structure undoubtedly controlled the fate of a nanoparticle after a sudden change in pH. For conjugates I, I-Dox, III, and III-Dox, a core was getting bigger with time, whereas for conjugates II, II-Dox, IV, and IV-Dox, the core size R_{sphere} was diminishing or remained nearly constant (Table 2).

Kinetics at Early Times (SANS). The structural changes at early times were elucidated by time-resolved neutron scattering experiments upon a rapid change in pH from 7.4 to 5. This change was achieved in a stopped-flow instrument. The scattering curves for the conjugate III reveal clear changes with time (Figure 8), indicating a structural transition in the

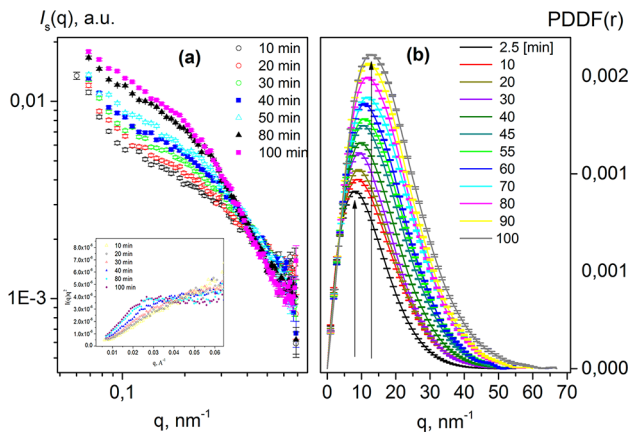


Figure 8. Time evolution of SANS curves (a, inset: Kratky plot) and PDDFs (b) for conjugate III.

system. The kinetics are very slow, in the time range of minutes or slower (hours), in agreement with the SAXS data reported above. The scattering curves from nanoparticles usually reveals several regions, and often $I \sim q^\alpha$ is encountered with characteristic behaviors for various length scales of the nanoparticle. Thus, the inner structure of the nanoparticles (compact or branched polymer structures) can be detected in the intermediate q range of a Kratky plot ($I(q)q^2$ vs q). For hard spheres, a pronounced maximum is followed by multiple peaks, whereas a plateau is observed for branched systems: $I(q)q^2$ for a polymer in Gaussian conformation steadily grows, reaching a plateau without any peak. The peak position is expected to be inversely proportional to the radius of gyration. The scattering curves for the conjugate III in the Kratky representation are provided for various times in Figure 8a, inset. Kratky representations unequivocally reveal structural differences for the conjugate as a function of time in the intermediate q range. The effect of the cholesterol derivative nature on the size of nanoparticles can best be observed in real space using the pair-distance distribution function. In Figure 8, the curves for conjugate III are presented. The PDDF curves clearly show that the radius of gyration (indicated with arrows) of nanoparticles, R_g , increases with time. Moreover, the values of R_g obtained from the fitting (Figure 6S) are in good agreement with the data reported earlier for SAXS measurement (Figure 2). The curves rise steeply with a pronounced maximum. The tail at higher r values becomes more asymmetric with time, that is, the nanoparticles evolve from a spherical to a more

ellipsoidal shape (Figure 6S). The SANS results show that these shape changes in conjugate III take place immediately after the change of pH and proceed within the first 1–2 h.

Large Aggregates (Dynamic Light Scattering (DLS)).

Dynamic light scattering was performed to determine the average size of the nanoparticles. DLS experiments are widely used for these purposes.^{33–41} Rigorous DLS experiments revealed that the nanoparticles previously reported on¹² are aggregates composed of free cholesterol derivatives (Figure 7S). The number of large aggregates is negligible in comparison with the amount of the nanoparticles themselves (Figure 7S, insets a,b).

DISCUSSION

To summarize, model independent approaches such as Guinier approximation, calculation of the PDDF, and ab initio methods evidently revealed the influence of spacer structure on the fate of a cholesterol derivative after a pH jump from 7.2 to 5. The R_g , D_{\max} Porod volume, and shape of PDDFs indicated that nanoparticles assembled from the conjugated $S\alpha$ -cholestan-3-one and Lev-Chol derivatives undoubtedly grew with time. The presence of Dox moieties in a conjugate had a minor impact on the kinetics of nanoparticle evolution. Generally, nanoparticles composed from I-Dox and III-Dox conjugates are larger than the ones for Dox-free conjugates for all time points. Further, the size difference diminished after 12 h from the pH change (Figures 2 (top left, bottom left) and 2S (top left, bottom left)). Such a phenomenon was easy to interpret, recalling the kinetics of Dox release reported for the conjugates in our previous paper.¹² Indeed, after 10–11 h at pH = 5, a vast majority of Dox was released from the conjugate. Thus, the coincidence of the sizes of Dox and Dox-free nanoparticles with $S\alpha$ -cholestan-3-one and Lev-Chol derivatives at the final stage was due to total elution of Dox particles from the polymeric micelles. A question that remained unanswered was why the nanoparticles grew instead of decompose. The unique feature observed from the PDDFs for conjugates I, I-Dox, III, and III-Dox helped to shed light on this matter. Namely, the kink that grew with time at $r = 2.5$ nm. The kink position implies the presence of cholesterol moieties in the shell. Indeed, the geometrical size of cholesterol correlates with observed peak position in the r -space.⁴² A similar shoulder in the PDDF was already observed for Waldenström immunoglobulin M (IgM) with a star conformation.⁴³ It was determined that the presence of star branches results in kink occurrence on PDDF. We can now postulate that the reason for the micelle growth discovered for $S\alpha$ -cholestan-3-one and Lev-Chol derivatives was continuous accumulation of cholesterol in the particle's outer shell. Ab initio results for conjugate I, where some bulky inhomogeneities spreading over the nanoparticle's surface with time were observed gave another indirect verification of our hypothesis. Model-dependent fitting further supported such postulation from the model-independent approaches. The presence of a shell consisting mainly of HPMA chains was witnessed from the fitting (Figure 6, Table 2). Calculated excess scattering lengths for core and shell undoubtedly highlighted their transformation (Figure 7). The core excess scattering length value at the end of the experiment is strikingly lower than that of shell. For conjugate I, one can even see the swapping of these two parameters with time. At the beginning, the core is denser than the shell; at the end it is the reverse (Figure 7). For conjugate I-Dox, the shell is denser than the core all the time. Such a finding is not surprising if we recall the properties of Dox

particles discovered in our previous work for conjugates with noncleavable cholesterol.⁹ It was established that Dox is distributed around the whole nanoparticle, not only in the core. Also, it was found that bulky Dox fragments disturb the core structure. Here we can generalize these findings and completely explain the time evolution of I-Dox and III-Dox nanoparticles. Dox particles that were entirely distributed over a nanoparticle disturb the core, which made it bigger than a Dox-free analogue. That observation differs from the one at pH 7.4, where nanoparticles with Dox are smaller than Dox-free ones due to additional tendency of tightly bound Dox moieties to contract.⁹ Dox molecules then eluted with time, resulting in a reduction of excess scattering length of the shell and core (Figure 7). At the final stage, excess scattering lengths of core and shell for Dox and Dox-free conjugates concisely indicated that the Dox elution process was complete. The difference in spacer structure for conjugates I and III resulted in different evolution of cholesterol derivatives inside the nanoparticle. For conjugate I, there was a sharp change in the core at the beginning, with a slower transfer process in a second phase. It is highly probable that 5α -cholestane-3-onecholestane-3-one (I) derivatives accumulate in the outer shell after cleaving a bit faster than Lev-chol (III) derivatives. SAXS measurements with a better time resolution are required to answer this question unambiguously. On the basis of all obtained data we can propose a hypothetical structure of the nanoparticle evolution in time (Figure 9a,b).

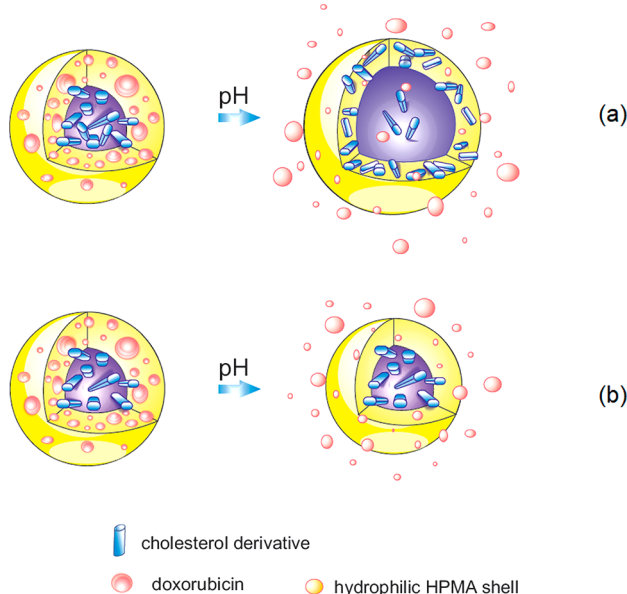


Figure 9. Hypothetical model of the structural evolution of nanoparticles composed of conjugates I-Dox and III-Dox (a), and IV-Dox (b) after a pH jump from 7.2 to 5.0.

Having established the mechanism of evolution from conjugates I and III, we can interpret the behavior of the other conjugates. Conjugate IV with cholest-4-en-3-one derivative is robust to changes in pH. Neither R_g , nor other physical-chemical parameters (D_{max} , PDDF, R_{core} , R_{chain}) change in time inside of experimental error. The explanation for that was already proposed in our previous paper.¹² We believe that the presence of conjugated double bonds in spacer structure (Figure 1) prevents the hydrazone bond from cleaving. This conclusion was further supported by time evolution of the IV-

Dox conjugate where decrease in size was observed with time. Moreover, the nanoparticles composed of IV-Dox conjugates are always smaller than IV ones. Apparently, only Dox elution is observed for this system. Fortunately, we were able to elucidate pure Dox release for that system (Figure 9, b). Obviously, cholest-4-en-3-one moieties stayed inside of the core resulting, unlike I, I-Dox, III, and III-Dox conjugates, in a core excess scattering length for the IV and IV-Dox system higher than that for shell disregarding time. This effect is even more pronounced for conjugates II and II-Dox (Table 2). In contrast with the other conjugates, there is a minor decrease in R_g , D_{max} , and Porod volume values (Figure 2 and 2S, top right), where II-Dox conjugates are slightly bigger than II ones. It is worth noting that the core excess scattering length for conjugates II has the highest value in comparison with other conjugates. Keeping in mind that the spacer in conjugate II has the highest hydrophobicity ($\log P$ value, Table 1) due to the presence of an additional benzene ring in the spacer structure, we could assume that the decrease in size observed for this conjugate came from additional packing of hydrophobic moieties with time after they were released. Thus, despite some similarities, different driving forces controlled the time evolution of conjugates II and IV. For conjugates II and II-Dox, hydrophobicity dictated the time evolution, whereas conjugated double bonds added stability for conjugates IV and IV-Dox.

Surprisingly, obtained data revealed completely different solution behavior for 5α -cholestane-3-onecholestane-3-one and Lev-Chol derivatives. We believe that the reason for that is their slightly lower hydrophobicity. We hypothesize that, after a hydrazone bond is broken, a single cholesterol moiety is subject to thermal motion that enables the migration of 5α -cholestane-3-onecholestane-3-one and Lev-Chol derivatives outside the core to a HPMA shell. We suppose that such derivatives that move to the shell could be at the origin of hydrophobic micro-domains which start to attract other derivatives into the shell, thus making the core less stable. Such cholesterol micro-domains are probably covered by hydrophilic HPMA chains that prevent the escape of the derivatives into the aqueous surrounding. This scenario is not realized for the Opb spacer due to its higher hydrophobicity.

We may also conclude that the peak corresponding to sizes of 50–100 nm observed by DLS for conjugates I, II, and III, in our previous paper, was erroneously attributed to true polymeric micelles. The true polymeric micelles (i.e., the nanoparticles) are much smaller, according to SAXS data. Larger particles observed previously¹² are therefore assigned to aggregates. We were able to disclose a peak (5–10 nm) related to the true polymeric micelles in the R_h distribution function although it has a very low amplitude in comparison with the amplitude from the aggregates (Figure 7S). Nevertheless, conversion of the intensity weighted distribution function to the number weighted distribution proves that the major population of particles in solution is true polymeric micelles.

CONCLUSIONS

The release of doxorubicin (Dox), an anticancer drug, from amphiphilic N-(2-hydroxypropyl) methacrylamide (HPMA)-based copolymers was characterized using time-dependent SAXS/SANS measurements after a pH jump simulating the particle transport from blood (pH = 7.4) to a tumor environment (pH = 5.0). To our best knowledge, we were able, for the first time, to monitor the change in properties of a drug delivery carrier with time in conditions mimicking the

tumor microenvironment by SAXS/SANS methods. For most conjugates, nanoparticle growth or decay was observed in the time range of several hours. It was established that the growth/decay rate and the steady-state size of nanoparticles depend on the spacer structure. We concluded that the spacer structure determines the fate of a cholesterol derivative after a pH jump. The elution of Dox from a nanoparticle was traced over time. Fitting results for 5α -cholestane-3-one and Lev-chol spacers implied that cholesterol moieties were continuously escaping from the nanoparticles core and concentrate in the hydrophilic shell. In contrast, the cholest-4-en-3-one spacer seemed to be stable in conditions mimicking tumor cells due to its conjugated double bonds, thus, preventing cholesterol escaping. Dox moiety release was only observed for the cholest-4-en-3-one spacer with change in pH. Such findings justify the model proposed in our previous paper. In reverse, micelles composed of Opb-spacers grew more compact with time due to its higher hydrophobicity.

ASSOCIATED CONTENT

Supporting Information

SAXS scattering curves for the conjugate I; Porod volumes for conjugates I, I-Dox, II, II-Dox, III, III-Dox, IV, and IV-Dox; Ab initio calculations for the conjugates I, I-Dox, and IV; R_h data for conjugate I; and SANS scattering curves for the conjugate III. This material is available free of charge via the Internet at <http://pubs.acs.org>.

AUTHOR INFORMATION

Corresponding Authors

*Tel.: +420-608720561. Fax: +420-296809410. E-mail: sfill225@gmail.com.

*Tel.: +490-4089902224. Fax: +490-4089902149. E-mail: konarev@embl-hamburg.de.

Notes

The authors declare no competing financial interest.

ACKNOWLEDGMENTS

M.D. thanks the MaMaSelf (Master in Materials Science Exploiting Large Scale Facilities) master program for financial support. The FRM-II is also acknowledged for beam time allocation. The authors acknowledge support from Grant Agency of the Czech Republic (Grant No. P208/10/1600). The authors acknowledge financial support from the European Commission under the Seventh Framework Program by means of the Grant Agreement for the Integrated Infrastructure Initiative No. 262348 European Soft Matter Infrastructure (ESMI). The authors also acknowledge financial support Nr. CZ09-DE06/2013-2014 from the ASCR-DAAD Programme PPP 2013-2014 and from German Bundesministerium für Bildung und Forschung Grant BioSCAT, Contract No. 05K12YE1.

REFERENCES

- Duncan, R.; Vicent, M. J. *Adv. Drug Delivery Rev.* **2013**, *65*, 60–70.
- Torchilin, V. P. *Cell. Mol. Life Sci.* **2004**, *61*, 2549–2559.
- Zhao, Y.; Alakhova, D. Y.; Kim, J. O.; Bronich, T. K.; Kabanov, A. V. *J. Controlled Release* **2013**, *168*, 61–69.
- Kopeek, J.; Kopekova, P. *Adv. Drug Delivery Rev.* **2010**, *62*, 122–149.
- Ulbrich, K.; Šubr, V. *Adv. Drug Delivery Rev.* **2010**, *62*, 150–166.
- Vicent, M. J.; Manzanaro, S.; de la Fuente, J. A.; Duncan, R. J. *Drug Targeting* **2004**, *12*, 503–515.
- Griffiths, P. C.; Paul, A.; Apostolovic, B.; Klok, H. A.; de Luca, E.; King, S. M.; Heenan, R. K. *J. Controlled Release* **2011**, *153*, 173–179.
- Etrych, T.; Chytil, P.; Mrkvan, T.; Širová, M.; Řehová, B.; Ulbrich, K. *J. Controlled Release* **2008**, *132*, 184–192.
- Filippov, S. K.; Chytil, P.; Konarev, P.; Dyakonova, M.; Papadakis, C.; Zhigunov, A.; Plestil, J.; Stepanek, P.; Etrych, T.; Ulbrich, K.; Svergun, D. *Biomacromolecules* **2012**, *13*, 2594–2604.
- Paul, A.; Vicent, M.; Duncan, R. *Biomacromolecules* **2007**, *8*, 1573–1579.
- Paul, A.; James, C.; Heenan, R. K.; Schweins, R. *Biomacromolecules* **2010**, *11*, 1978–1982.
- Chytil, P.; Etrych, T.; Kostka, L.; Ulbrich, K. *Macromol. Chem. Phys.* **2012**, *213*, 858–867.
- Pedersen, J.; Svaneborg, C.; Almdal, K.; Hamley, I.; Young, R. *Macromolecules* **2003**, *36*, 416–433.
- Angelov, B.; Angelova, A.; Filippov, S.; Karlsson, G.; Terrill, N.; Lesieur, S.; Stepanek, P. *Soft Matter* **2011**, *7*, 9714–9720.
- Stepanek, M.; Matejcek, P.; Prochazka, K.; Filippov, S.; Angelov, B.; Slouf, M.; Mountrichas, G.; Pispas, S. *Langmuir* **2011**, *27*, 5275–5281.
- Blanchet, C.; Zozulya, A.; Kikhney, A.; Franke, D.; Konarev, P.; Shang, W.; Klaering, R.; Robrahn, B.; Hermes, C.; Cipriani, F.; Svergun, D.; Roessle, M. *J. Appl. Crystallogr.* **2012**, *45*, 489–495.
- Konarev, P.; Volkov, V.; Sokolova, A.; Koch, M.; Svergun, D. J. *J. Appl. Crystallogr.* **2003**, *36*, 1277–1282.
- Guinier, A. *Small-Angle Scattering of X-rays*; Wiley: New York, U.S.A., 1955.
- Svergun, D. *J. Appl. Crystallogr.* **1992**, *25*, 495–503.
- Franke, D.; Svergun, D. *J. Appl. Crystallogr.* **2009**, *42*, 342–346.
- Svergun, D. *Biophys. J.* **1999**, *76*, 2879–2886.
- Volkov, V.; Svergun, D. *J. Appl. Crystallogr.* **2003**, *36*, 860–864.
- Kozin, M.; Svergun, D. *J. Appl. Crystallogr.* **2001**, *34*, 33–41.
- Glatter, O.; Kratky, O. *Small-Angle X-ray Scattering*; Academic Press: New York, U.S.A., 1982.
- Glatter, O. *J. Appl. Crystallogr.* **2000**, *33*, 218–233.
- Pedersen, J. S.; Gerstenberg, M. C. *Macromolecules* **1996**, *29*, 1363–1365.
- Pedersen, J. S. *J. Appl. Crystallogr.* **2000**, *33*, 637–640.
- <https://kur.web.psi.ch/sans1/SANSSoft/sasfit.html>.
- Jakes, J. *Czech. J. Phys. (Paris)* **1988**, *38*, 1305–1316.
- Stepanek, P. Data analysis in dynamic light scattering. In *Dynamic Light Scattering: The Method and Some Applications*; Brown, W., Ed.; Clarendon Press: Oxford, U.K., 1993; pp 175–241.
- Svergun, D. *J. Appl. Crystallogr.* **2007**, *40*, S10–S17.
- Kirkpatrick, S.; Gelatt, C.; Vecchi, M. P. *Science* **1983**, *220*, 671–680.
- Konak, C.; Panek, J.; Hruby, M. *Colloid Polym. Sci.* **2007**, *285*, 1433–1439.
- Filippov, S.; Hruby, M.; Konak, C.; Mackova, H.; Spirkova, M.; Stepanek, P. *Langmuir* **2008**, *24*, 9295–9301.
- Hruby, M.; Filippov, S.; Panek, J.; Novakova, M.; Mackova, H.; Kucka, J.; Vetcicka, D.; Ulbrich, K. *Macromol. Biosci.* **2010**, *10*, 916–924.
- Filippov, S.; Konak, C.; Kopeckova, P.; Starovoytova, L.; Spirkova, M.; Stepanek, P. *Langmuir* **2010**, *26*, 4999–5006.
- Skodova, M.; Hruby, M.; Filippov, S.; Karlsson, G.; Mackova, H.; Spirkova, M.; Kankova, D.; Steinhart, M.; Stepanek, P.; Ulbrich, K. *Macromol. Chem. Phys.* **2011**, *212*, 2339–2348.
- Filippov, S.; Lezov, A.; Sergeeva, O.; Olifirentko, A.; Lesnichin, S.; Domnina, N.; Komarova, E.; Almgren, M.; Karlsson, G.; Stepanek, P. *Eur. Polym. J.* **2008**, *44*, 3361–3369.
- Gromadzki, D.; Filippov, S.; Netopilik, M.; Makuska, R.; Jigounov, A.; Plestil, J.; Horsky, J.; Stepanek, P. *Eur. Polym. J.* **2009**, *45*, 1748–1758.
- Filippov, S.; Starovoytova, L.; Konak, C.; Hruby, M.; Mackova, H.; Karlsson, G.; Stepanek, P. *Langmuir* **2010**, *26*, 14450–14457.

(41) Panek, J.; Filippov, S.; Hraby, M.; Kucka, J.; Rabyk, M.; Bogomolova, A.; Stepanek, P. *Macromol. Rapid Commun.* **2012**, *33*, 1683–1689.

(42) Hosta-Rigau, L.; Zhang, Y.; Teo, B.; Postma, A.; Staedler, B. *Nanoscale* **2013**, *5*, 89–109.

(43) Wilhelm, P.; Pilz, I.; Palm, W.; Bauer, K. *Eur. J. Biochem.* **1978**, *84*, 457–463.